# Characterizing Cislunar Fragmentations

**Arly Black**
*School of Aeronautics and Astronautics, Purdue University*
*black99@purdue.edu*
**Carolin Frueh**
*School of Aeronautics and Astronautics, Purdue University*
*cfrueh@purdue.edu*

## ABSTRACT

Fragmentation debris in the cislunar region creates enormous space situational awareness complications in an already chaotic domain. With heightened international interest in spacecraft activities in the vicinity of the Moon, an exponential increase in cislunar space debris is likely to follow. Even one fragmentation event can have catastrophic and far-reaching consequences, which drives the need for appropriate debris characterization tools. This work investigates patterns in fragment behavior as a function of energy level and orbit location, and explores emergent dynamic structures in the vicinity of the Earth-Moon $L_2$ Lagrange point. A modified version of the NASA-developed Standard Breakup Model is employed in the analysis of a realistic breakup event, and results are compared against the pattern of behavior discovered in the earlier analysis.

## 1. INTRODUCTION

Cislunar space, the region beyond the geostationary belt of near-Earth objects up to the lunar sphere of influence, has increasingly become of interest for mission designers and spacecraft operations [1]. Recent and prospective missions include CNSA's Chang'e series of orbiters, landers, and rovers, ISRO's Chandrayaan-3 mission to the lunar south pole, the CAPSTONE technology demonstration satellite to an $L_2$ NRHO, and NASA's crewed Artemis program [2, 3, 4]. An increase in activity in this area heightens the risk of fragmentation events, through collisions, failed passivation of propellant tanks, battery explosions, or deterioration of aging or damaged spacecraft, among other causes. Debris generated from such events may be hazardous to the safe operation of active satellites, in not only cislunar orbits, but near-Earth orbits as well, adding to an already precariously congested region [5]. The remoteness and large volume of the cislunar domain introduces additional observation and tracking challenges which complicate crucial Space Domain Awareness (SDA) activities. This, then, requires a comprehensive grasp of spacecraft breakup behavior and dynamics.

The challenge when evaluating breakup events in the cislunar region is that the parameter space is vast. This holds true even when employing the circular restricted three-body problem (CR3BP), which is considered relatively computationally inexpensive, and excluding other relevant forces such as solar radiation pressure and gravitational effects of Jupiter and the Sun. Fragmentation events differ by: type and intensity; mass of the parent object; number, size, and energy of generated fragments; the trajectory or orbital family on which the event takes place (planar, non-planar, transfer, etc); and where on a given trajectory the event occurs, to name a few factors [6]. Because of the immense scope of this problem, researchers have tended towards exploration of single instance fragmentation cases, such as events occurring on select members of the Lyapunov or Halo orbital families [7, 8, 9]. This first series of papers show impressively how widespread the impacts of a single collision can be and that fragments may easily migrate onto trajectories that interact with the near-Earth region, including Low and Medium Earth orbits and Geosynchronous orbits.

Tremendous computational resources have been expended to even glimpse at a subset of possibilities in a single orbital family [8]. However, given the chaotic nature of the system dynamics in this region, nearby cases may exhibit entirely different behavior. Thus, many of the relevant scenarios remain unexplored and no method so far exists to survey the parameter space or to extrapolate from a given set of initial conditions to a different, even neighboring, set of initial conditions.

In this paper, we introduce methods to characterize the behavior of debris fragments over a range of parameters near the Earth-Moon $L_2$ region of cislunar space without the need for extensive propagation. Section 2 provides a brief review of CR3BP dynamics and some of the key related topics drawn upon in this study. Section 3 describes modifications made to the NASA Standard Breakup Model for the following investigation. Section 4 discusses results of case studies on constant energy breakup events, the influence of location within an orbit on fragmentation outcomes, and a physically realistic explosion scenario. Finally, we will offer some conclusions extracted from the results of this study.

## 2. DYNAMICAL MODEL

### 2.1 Circular Restricted Three Body Problem

When describing the dynamics of objects in cislunar space, it is insufficient to employ near-Earth two-body orbital mechanics, as gravitational effects of both the Earth and Moon must be considered. The Circular Restricted Three Body Problem (CR3BP) is a simplified model that enables computationally efficient insight into cislunar trajectory dynamics [10]. Expressed in a non-dimensional, rotating reference frame, the CR3BP reflects the motion of an infinitesimal particle under the gravitational influence of two massive primary bodies which rotate in circular orbits about their mutual barycenter at a constant rate. The governing second-order, coupled, nonlinear equations of motion for a spacecraft under these conditions are

$$\ddot{x} = 2\dot{y} + \frac{\partial U^*}{\partial x} \qquad \ddot{y} = -2\dot{x} + \frac{\partial U^*}{\partial y} \qquad \ddot{z} = \frac{\partial U^*}{\partial z}, \tag{1}$$

where $x, y, z$ and their derivatives represent the coordinates associated with the Earth-Moon rotating frame, such that the $x$-axis is directed along the vector from the Earth to the Moon, and the $z$ direction is normal to the Earth-Moon rotating plane. $U^*$ is the gravitational pseudo-potential associated with the system, defined as

$$U^* = \frac{1}{2}(x^2 + y^2) + \frac{\mu}{d} + \frac{1-\mu}{r}. \tag{2}$$

Parameters $d$ and $r$ represent the distances between the Earth and the spacecraft, and the Moon and the spacecraft, respectively, while $\mu$ is the non-dimensional mass constant of the system. The non-dimensional distance between primaries is set to unity.

Although the CR3BP does not admit a general closed-form analytical solution, it is possible to seek out particular solutions, by identifying locations with zero initial velocity or acceleration with respect to the rotating frame, such that gravitational and centrifugal forces cancel. This yields five equilibrium positions, known as Lagrange or libration points $L_i$ for $i = 1, ..., 5$, which all lie in the rotating plane of motion of the primaries. The CR3BP does additionally concede a single integral of the motion, a constant energy-like quantity referred to as the Jacobi constant *JC*, defined as

$$JC = 2U^* - \sqrt{\dot{x}^2 + \dot{y}^2 + \dot{z}^2}, \tag{3}$$

where the second term represents the magnitude of the spacecraft velocity in the rotating frame, and the value of *JC* is inversely proportional to the energy of the orbiting third body. This constant restricts the motion of the third body to physically accessible regions of travel, such that the magnitude of the velocity in the rotating frame is not imaginary. When the velocity is reduced to zero, this yields a continuous surface that defines a boundary that cannot be crossed ballistically, given the energy of the spacecraft. This forbidden boundary is known as a Zero Velocity Surface (ZVS), or Zero Velocity Curve (ZVC) in the planar case. As energy increases, ZVS volumes are reduced and objects are able to move more freely through cislunar space. The *JC* values that correspond to the ZVCs that pass through each $L_i$ are listed in Table 1. In other words, these values indicate the *JC* at which a given Lagrange point 'gateway' opens and becomes accessible for a spacecraft to pass through.

Table 1: Nondimensional Jacobi constants associated with the Earth-Moon libration points.

| | $L_1$ | $L_2$ | $L_3$ | $L_{4/5}$ |
|---|---|---|---|---|
| *JC* [nd] | 3.1883 | 3.1722 | 3.0121 | 2.9880 |

### 2.2 Libration Point Orbits

Around each of the respective Lagrange points, there exist families of periodic or quasi-periodic libration point orbits (LPO) which can be advantageously leveraged in cislunar mission design. A periodic orbit is one that consistently repeats itself over a constant time period, while quasi-periodic orbits reside on invariant tori about their corresponding periodic orbits. In the Earth-Moon domain, LPOs include Lyapunov and Distant Retrograde Orbits (DRO), which lie entirely in the plane of the two primary bodies, as well as Halo, Vertical, Axial, and Lissajous orbits, among others, which contain out-of-plane components. Orbits revolving the collinear libration points $L_1$, $L_2$, and $L_3$, which lie along the line connecting the two primaries, are considered dynamically unstable, in that even small deviations from an equilibrium state grow continuously over time. Equilateral LPOs (around $L_4$, $L_5$), on the other hand, are deemed stable, and do not require station-keeping to remain in the Lagrange point vicinity.

Earth-Moon $L_2$ orbits have emerged as attractive destinations for space station and lunar surveillance orbits: an $L_2$ southern halo orbit has been used by the Chinese Queqiao relay satellite to enable communication with their Chang'e 4 lunar lander on the far side of the Moon [3], while the CAPSTONE mission operates in a southern Near Rectilinear Halo Orbit (NHRO) as a precursor and validation mission for NASA's Artemis Gateway lunar orbital platform [4]. Additionally, the existence of manifolds in the $L_2$ vicinity offers natural arrival and departure pathways, convenient for low-cost travel to this region. For simplicity, this investigation is focused on members of the $L_2$ planar Lyapunov orbit family, a subset of which are shown in Figure 1, along with their associated Jacobi constants.

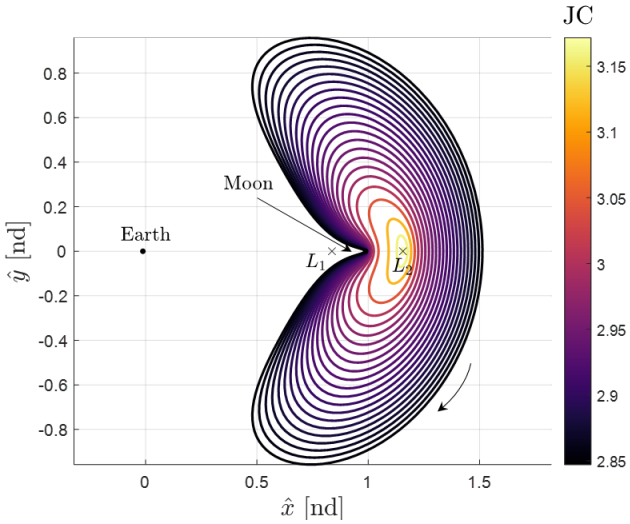


Fig. 1: $L_2$ Lyapunov family members in the non-dimensional Earth-Moon system, color-coded by Jacobi constant. The arrow indicates the orbital direction of motion.

### 2.3 Poincaré Maps

Because the phase space dimensionality is vast, lower dimensional visualizations can enable us to extract more meaningful information from a trajectory. Poincaré maps are a method of reducing the dimensionality of a state space by converting a continuous flow to a discrete-time representation, in order to enable identification of patterns or structures in the emergent behavior. Poincaré sections are defined transverse to the flow of the system, such that the trajectory has some component normal to the hyperplane $\Sigma$, and returns to $\Sigma$ are recorded from one of either the positive or negative directions (one-sided) or both directions (double-sided). Poincaré maps tend to exhibit certain properties unique to periodic and quasi-periodic orbits and provide clarity regarding the global dynamics of a system. Note that Poincaré maps track points that may not necessarily return to the map at the same time; however, a different class of maps, known as stroboscopic maps, exist where the sampling frequency matches the period of a given orbit. Poincaré maps may be further reduced in dimension by restricting the Jacobi value.

## 3. DEBRIS BREAKUP MODEL

Collision and explosion breakup prediction models are a crucial component of any debris environment tool. The NASA Standard Breakup Model (SBM) [6] is the most commonly embraced breakup model. This semi-empirical and statistical application, developed in the late 1990s, was modeled around existing on-orbit collision and explosion data at the time, as well as controlled ground-test data. The SBM provides three fundamental outputs for each generated fragment: size $L_c$, area-to-mass ratio $AM$, and relative velocity $\Delta V$ distributions.

While the main procedures, formulas, and distribution functions are publicly available through published documentation, the descriptions are not entirely comprehensive, and attempts in this work to fill in the gaps are speculative. Although the original publication does not provide mass or momentum conservation controls, a later update describes a mass conservation technique [11]. Momentum conservation is assured in the present work through the application of a scale factor to each fragment velocity vector. The delta-v direction for each fragment is another unknown, which is assumed here to be determined via a uniform distribution of unit vectors on a sphere. This assumption therefore implies that the model does not consider non-isotropic explosions or asymmetrical collisions. The customized version employed in this work additionally includes some modifications implemented by ESA's MASTER-8 version of the SBM [12]. These include the addition of a bridging function between the large and small particle area-to-mass ratio models, clarifications on the area-to-mass and velocity probability density functions, and a correction to the area-to-mass distribution for spacecraft particle sizes below 1 mm. Finally, when computing the number of generated fragments in explosion cases, the original estimation does not consider the mass of the exploding object but rather relies on a scaling factor $s$, such that the number of explosive fragments of size $L_c$ or larger is $N = s \cdot 6 \cdot L_c^{-1.6}$. In the documentation, the only value provided for $s$ is 1 for rocket bodies with masses between 600 to 1000 kg [6]. However, this value is not always appropriate for all objects of this type or objects of other masses. If $s$ is too large, the sum of the produced fragments can be greater than the mass of the original spacecraft, and conservation of mass will yield fragments with negative masses. If $s$ is too small, the model will produce a few fragments with overly large masses. Other works empirically determine appropriate $s$ values on a case-by-case basis, but do not provide values for purely numerical cases [12]. Therefore, the modified model used here has implemented an optimization scheme to determine the appropriate scaling factor for any given mass, such that the sum of the generated fragments is less than, but reasonably close to (within 15%) the mass of the original target object. This represents an explosion with a relatively uniform fragment dispersion, although the optimization parameters may be updated in the future to examine nonuniform cases. Further details on the optimizer are discussed in Section 4.2.1. The SBM version used in the following analysis was adapted by the authors of this work specifically for this investigation, and will hereafter be referred to as the 'modified SBM'.

## 4. CISLUNAR FRAGMENTATION PATTERNS

Given the extensive parameter space involved in fragmentation analysis, the isolation of certain key characteristics can be leveraged to evaluate their individual influences on fragment dynamics and feasible regions of travel. The first part of the study explores theoretical constant Jacobi fragmentation events, such that every generated fragment possesses the same energy. The second investigation employs the modified SBM to explore a parameter sensitivity study and simulate a realistic explosion event.

### 4.1 Constant Energy Analysis

Although a fragmentation event that solely produces debris with fixed energies is physically unrealistic, evaluation of such theoretical simulations can provide insight into the behavior of objects with those energies in a practical scenario. We consider a hypothetical satellite traveling along a given Earth-Moon $L_2$ Lyapunov orbit, subject to an isotropic explosion, such that all generated fragments are ejected symmetrically in all directions. If the energy of each fragment is constrained to a constant Jacobi value, the final velocity of each fragment can be determined from equation 3. Note that not every fragment direction will be feasible, given the forbidden regions associated with the chosen $JC$.

#### 4.1.1 *Single fragmentation location cases*

For an object with an initial nondimensional position and velocity state of [1.2187 0 0 0 -0.4232 0], traveling on an orbit with $JC$ equal to 3.0165, and a period of around 18.54 days, as illustrated in Figure 2(a), we can examine the

outcome for fragments with constant energy levels in a few different cases. 998 equidistant ejection directions around a sphere are considered, and those fragments that cannot achieve the Jacobi constant of interest are eliminated. *JC*s of 2.99, 3.015, and 3.12 are selected to represent values near those associated with the Earth-Moon libration points, as given in Table 1, while maintaining $L_2$ accessibility. Recall that based on the notation used in this work, a higher Jacobi constant indicates a lower orbital energy, and thus a more limited region of travel. Fragments are generated at the selected location on the orbit and are propagated over a 30-day duration, as shown in Figure 2(b).

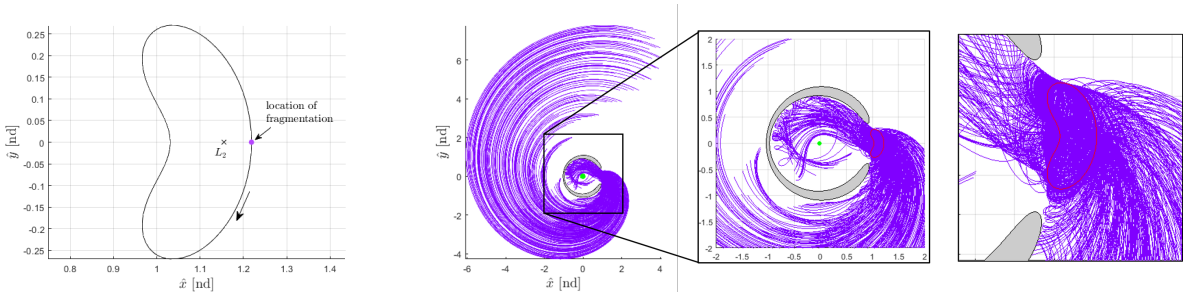


(a) Originating orbit and location of fragmentation event.

(b) Fragment trajectories over 1 month. Green marker indicates Earth; gray shaded area indicates forbidden region from the ZVC; red outline represents original orbit.

Fig. 2: (a) Single location of fragmentation event on an $L_2$ Lyapunov orbit with $JC = 3.0165$. (b) Fragment trajectories over a 30-day propagation.

Two-dimensional, double-sided, $y$-$z$ Poincaré maps in positional space are placed at the $L_2$ Lagrange point ($x = 1.1557$ nd), the Moon ($x = 0.9878$ nd), and the halfway point between $L_2$ and the Earth ($x = 0.5718$ nd) to investigate emergent patterns in those regions. Figure 3 shows the results of a comparison between the fragment patterns on each hyperplane for the same event, for fragments with a Jacobi constant of 3.015. This *JC* indicates that both $L_1$ and $L_2$ are open and accessible, while $L_3$ remains closed for travel. As seen in Figure 2(b), after generation, fragments either travel to the 'left' or 'right' of the original $L_2$ Lyapunov orbit, along what appear to be invariant manifolds or conduits that transport objects between primary bodies [13]. In two-dimensional space, manifolds have been mathematically proven to act as a separatrix or boundary between domains with distinct dynamical behavior. In three-dimensional space, invariant manifolds are empirically observed to act in a similar manner [13, 14], and this is seen here. Additionally, we observe that fragments that pass through the ZVC opening, through $L_2$ and then $L_1$, are unable to traverse through the boundaries of the shaded ZVC, as expected.

The purple markers in Figures 3(a)-(c) indicate the first time a fragment trajectory intersects with the respective maps, while the magenta markers indicate all subsequent returns to the maps. We observe three distinct neighborhoods in each map, shown in the left images of Figures 3(a)-(c), which represent (i) trajectories trapped inside the ZVC, referred to here as *inner fragments*, (ii) those that travel around and beneath the ZVC, hereafter referred to as *outer fragments*, and (iii) those that return to the map above the ZVC, which we will call *returned fragments*. Note that the *returned fragments* are the same objects as the *outer fragments*, but have simply traveled far enough to return to the map. Within those regions, fragments appear to form recognizable egg-like shapes symmetric about the $y$-axis. We can infer from this that the fragments are traveling along unstable invariant manifold tubes, consistent with our understanding of object dynamics in the vicinity of Lagrange points. From this perspective, it is clear that fragment movement is not confined to the plane of the original planar Lyapunov orbit, but expands in the z-direction as well. Compared to when the *outer fragments* first hit the map, when they reappear as *returned fragments*, their manifold is almost double in size, giving a clear image of the widespread impacts of such an event.

Zooming in on the maps, as shown in the right-side images of Figures 3(a)-(c), to the smaller manifold regions showing only the *inner* and *outer fragments*, we see that the percent of fragments that return to the map varies depending on where the map is located. Very few fragments (around 12.83%) return to the map between the Earth and $L_2$, although based on the pattern of the manifold, more fragments are likely to return given a longer propagation. Most of the returns appear to occur outside of the ZVC. The most returns occur at the Moon, at a percentage of around 73.35, while around 58.72% of fragments return to the hyperplane located at $L_2$.

Figure 4 illustrates the difference between fragment patterns of different constant energy levels, on a hyperplane

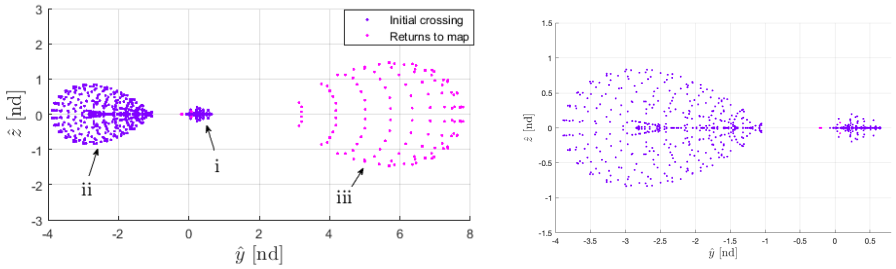


(a) Hyperplane at halfway point between Earth and $L_2$ ($x = 0.5718$ nd).

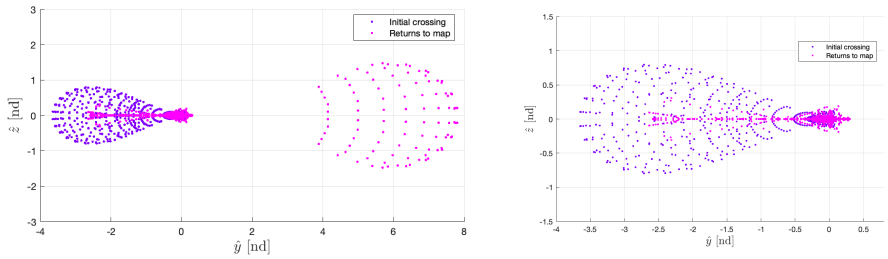


(b) Hyperplane at Moon ($x = 0.9878$ nd).

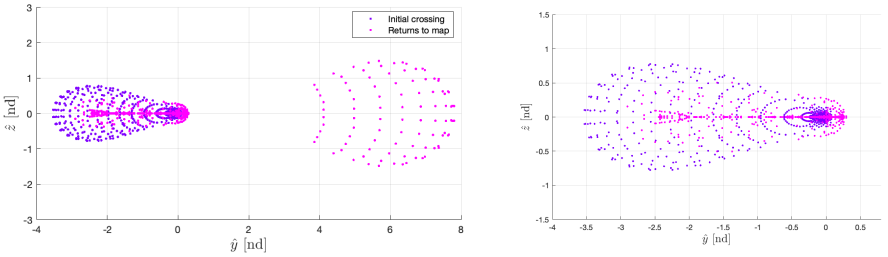


(c) Hyperplane at $L_2$ ($x = 1.1557$ nd).

Fig. 3: Comparison between Poincaré map intersections for fragments with $JC = 3.015$ at different locations along the Earth-Moon $x$-axis. Images on the right represent zoomed in portions of the map.

located at the halfway point between the Earth and $L_2$. With such a narrow gateway open at $L_2$ for a $JC$ of 3.12, very few fragments are able to make it through the ZVC corridor, which we can see clearly in the trajectory plot on the far left in Figure 4(a) and maps in the middle and right in Figure 4(a). This, once again, signifies that the energy is too low to traverse through the ZVC region. Additionally, many fragment directions of travel at this energy level are infeasible, and only 124 out of a possible 998 can be physically realized. In contrast, fragments with Jacobi constants of 3.015 or 2.99 are all viable, given the larger ZVC gateways, as seen in Figures 4(b) and (c). Furthermore, the qualifying fragments with $JC$ equal to 3.12 in Figure 4(a) appear to travel on a much narrower manifold tube than the other two cases. While it may not look like much from the plots, a non-dimensional distance of 1 is equal to the distance between the Earth and the Moon. Therefore the higher energy fragments can spread up to 384,400 km farther than the lower ones. Once again, we observe fragments in Figure 4(b) with $JC$ of 3.015 become trapped within the ZVC, while those in Figure 4(c) with $JC$ of 2.99 can travel virtually unimpeded by forbidden regions. While ZVCs are a great tool for limiting the available pathways of fragment travel in debris prediction analysis, so too are manifolds, as Figure 4(c) shows a clear structural corridor even without a large restrictive ZVC boundary.

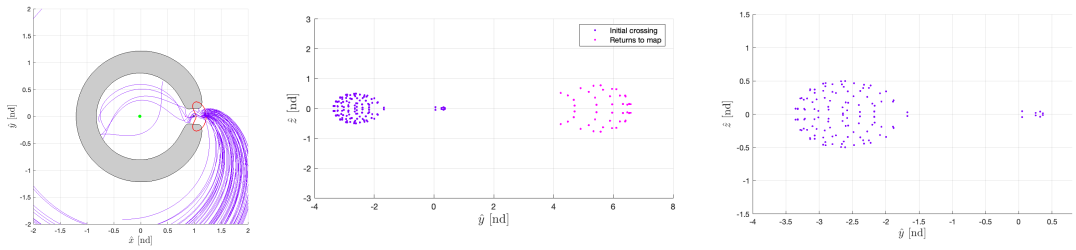


(a) $JC = 3.12$, 124 viable fragments.

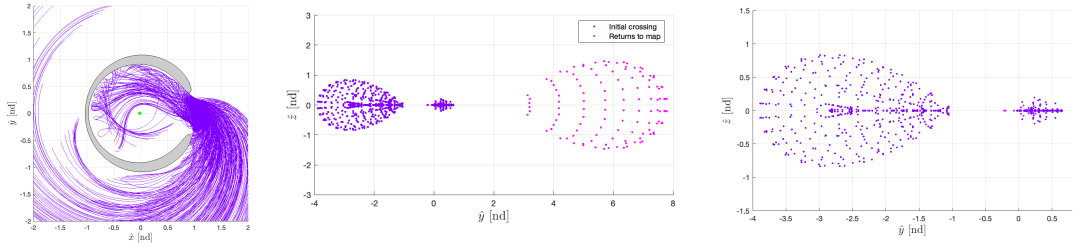


(b) $JC = 3.015$, 998 viable fragments.

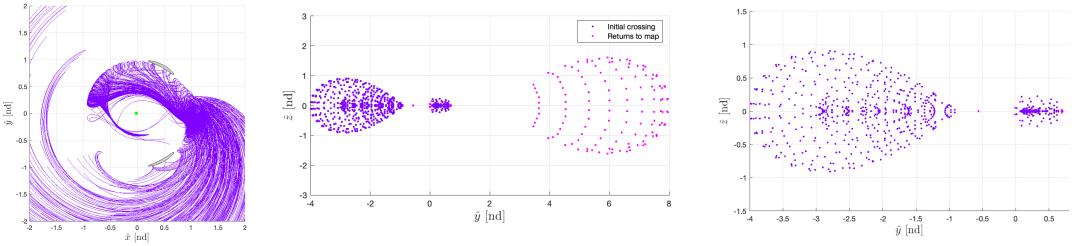


(c) $JC = 2.99$, 998 viable fragments.

Fig. 4: Comparison of fragments with Jacobi constants (a) 3.12, (b) 3.015, and (c) 2.99 on a Poincaré map located at the halfway point between the Earth and $L_2$ at $x = 0.5718$ nd. The rightmost figured provide a zoomed in view of the center figures.

### 4.1.2 *Multiple fragmentation location cases*

Advancing further in the investigation, the influence of the location of breakup on a given orbit is examined. Fragmentations at twenty equally spaced locations around the same orbit, as shown in Figure 5(a), are evaluated. The locations are defined based on their arc angle, or 'true anomaly' $\theta$, relative to the $L_2$ point, in degrees. As the spacecraft travels clockwise around the orbit, it traverses through negative $\theta$ angles first, which indicate a negative $y$-location in the Earth-Moon rotating system. Each location is color-coded according to $\theta$, as demonstrated in Figure 5(a). We can again compare fragments with different Jacobi constants, and additionally different initial orbits. We consider two different originating $L_2$ Lyapunov orbits, shown in Figure 5(a), and three sets of constant fragment $JC$s, whose associated ZVCs are displayed in Figure 5(b). Figure 6 examines fragments originating on an orbit with a $JC$ of 3.0165 that have three different constant energy levels. Through Poincaré maps and bar plots indicating the number of fragments from each starting location in each manifold, the figure enables a correlation between energy levels. Figure 7 displays a similar scenario but for fragments on a starting orbit with a $JC$ of 2.99. These figures together enable a comparison between disparate orbits. Figures 6(a) and 7(a) reveal hyperplane crossings at the halfway point between $L_2$ and the Earth for each of the orbits and prescribed locations. Returns to the map are not recorded this time.

We observe that the location of the fragmentation event around an orbit plays a significant role in dictating the regions of cislunar space that objects can traverse. Naturally, we can distinguish that as both the energy of the original orbit and the energy of the fragments increase, the fragment trajectory distances correspondingly increase as well. The

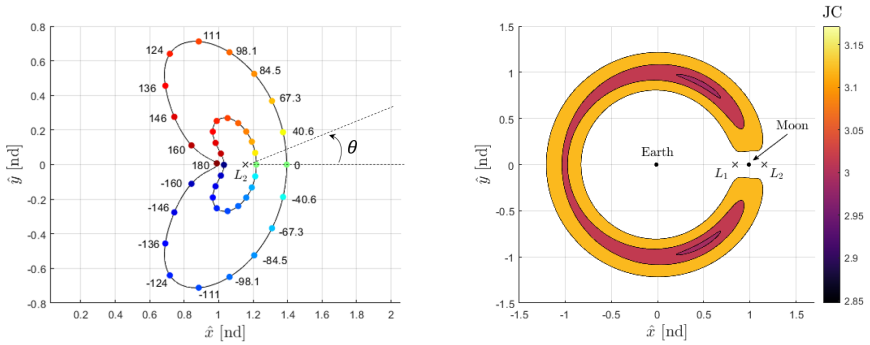


(a) Breakup locations, referenced by angle $\theta$. Small orbit $JC$ = 3.1065, large orbit $JC$ = 2.9001.

(b) ZVCs for $JC$s of 2.99, 3.015, and 3.12.

Fig. 5: (a) Originating orbits and locations of breakup events and (b) ZVC boundaries associated with the fragment Jacobi energies of interest.

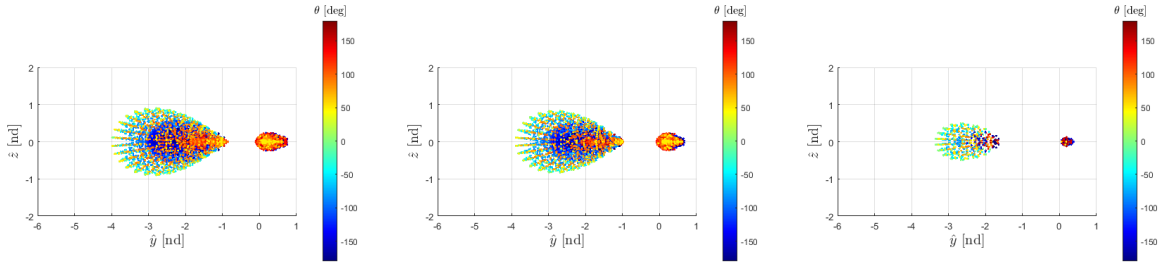


(a) Poincaré maps for fragments with constant $JC$ values of (left) 2.99, (middle) 3.015, and (right) 3.12.

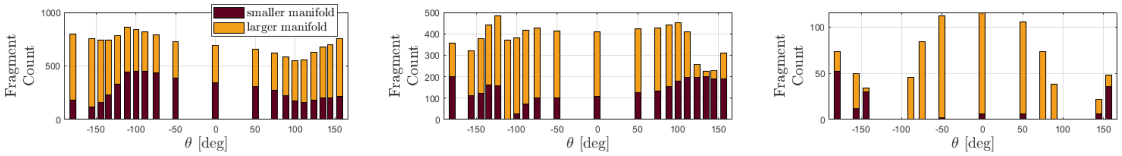


(b) Fragment counts indicating the number of fragments in either the larger manifold (yellow) or smaller manifold (maroon), corresponding to the plots in (a) for constant fragment $JC$ values of (left) 2.99, (middle) 3.015, and (right) 3.12.

Fig. 6: Comparison between (a) Poincaré map intersections for fragmentation events with three different constant $JC$s values on twenty locations around an orbit with $JC$ = 3.0165, and (b) the corresponding number of fragments that travel to either the larger or smaller manifold structures.

fragments that spread out the farthest distances in all cases appear to be those that are generated at $\theta$ angles of around $\pm 50^\circ$, which show up as the cyan, green, and yellow markers on the respective maps. On the other hand, fragments that originate at $\theta$ angles greater than $150^\circ$ and less than $-150^\circ$ appear to create manifolds with smaller diameters, and therefore less volume. Furthermore, Figures 6(b) and 7(b) reveal that fragments originating at $\theta$ angle locations symmetric about the $x$-axis do not necessarily produce similar results. These figures indicate the number of fragments at each location that travel to either the larger manifold outside of the ZVC, represented by the yellow portion of the bar plot, or to the smaller manifold inside the associated ZVCs, represented by the maroon portion of the bar plot. In Figure 6(b), which represents the chosen pathways of fragments that originate on the smaller orbit, we see a large disparity in where fragments end up between different energy levels. However, all three energy levels for the larger orbit follow a similar pattern, despite differences in the numbers of feasible fragments, as shown in Figure 7(b). Here we see that almost all fragments that originate in the angle range of $\pm 120^\circ$ end up in the larger manifold outside of the ZVC.

To get a clearer view of the impact of the starting orbit, we can overlay the results of multiple orbits on the same figure. By outlining the circumference of the maps of each orbit, the traversed volumes of cislunar space become more

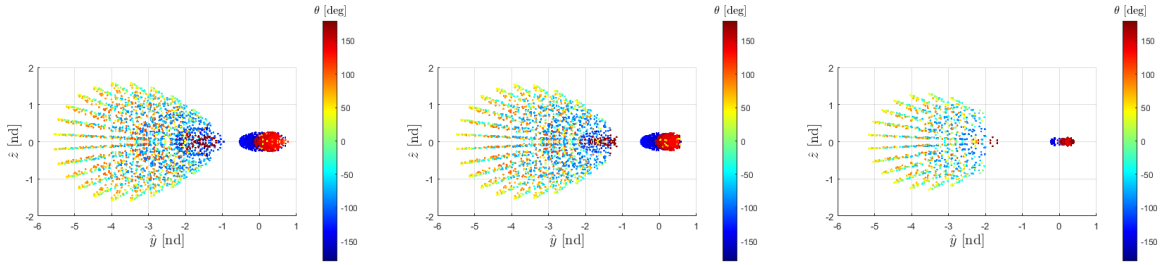


(a) Poincaré maps for fragments with constant *JC* values of (left) 2.99, (middle) 3.015, and (right) 3.12.

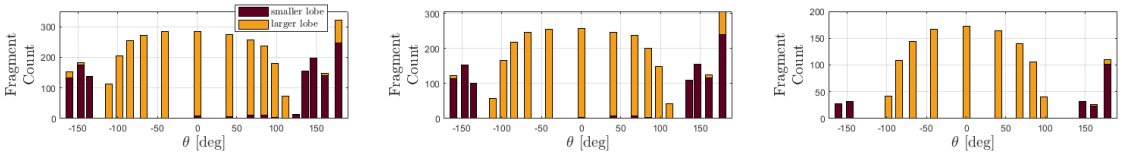


(b) Fragment counts indicating the number of fragments in either the larger manifold (yellow) or smaller manifold (maroon), corresponding to the plots in (a) for constant fragment *JC* values of (left) 2.99, (middle) 3.015, and (right) 3.12.

Fig. 7: Comparison between (a) Poincaré map intersections for fragmentation events with three different constant *JC*s values on twenty locations around an orbit with $JC = 2.9001$, and (b) the corresponding number of fragments that travel to either the larger or smaller manifold structures.

apparent. Figure 8 reveals manifold shapes associated with nine different orbits, shown with their color-codings in Figure 8(a), based on fragmentation events at twenty locations around each orbit. Once again, as energy increases, or *JC* decreases, more area is open to the fragments to move around. This can be observed most prominently for fragments originating in the smaller $L_2$ Lyapunov orbits (blue and green orbits), as we see the manifold diameter increase from *JC* of 3.12 in Figure 8(a) to 3.015 in Figure 8(b) and 2.99 in Figure 8(c). Thus the investigation reveals that both orbit and location on an orbit play a significant role in the outcome of a fragmentation event in the vicinity of the $L_2$ Lyapunov orbit.

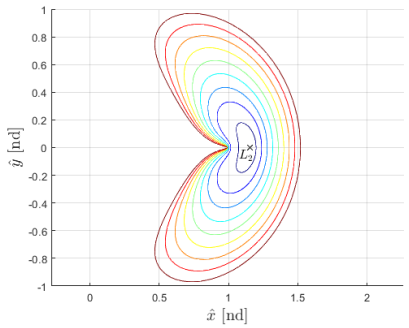


(a) color-coding map for each initial orbit

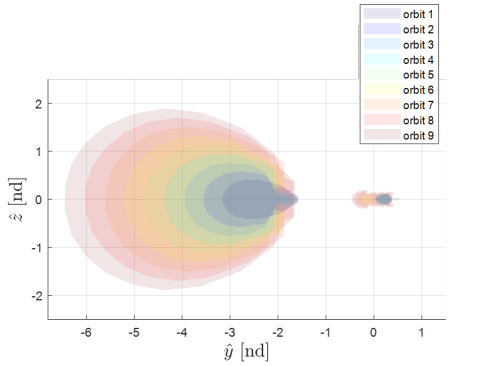


(b) Manifold cross-sectional areas for objects with $JC = 3.12$

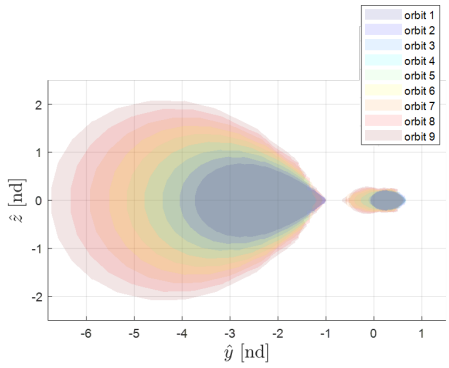


(c) Manifold cross-sectional areas for objects with $JC = 3.015$

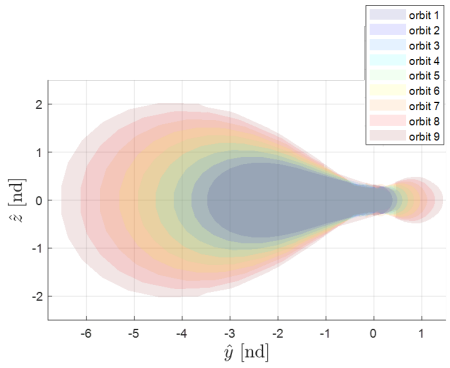


(d) Manifold cross-sectional areas for objects with $JC = 2.99$

Fig. 8: Comparison between boundaries of manifold cross-sections for objects with different constant energy levels, originating on 9 different orbits and 20 locations around the orbit.

### 4.2 Realistic Breakup Event

The modified satellite breakup model enables analysis of collision and explosion fragmentation events in orbit through the computation of fragment counts, sizes, area-to-mass ratios, and relative velocities. The model generates statistical distributions as a function of characteristic fragment length $L_c$. In the original SBM publication, the authors assert that the initial conditions of the breakup are 'highly influential' in the outcome of the model [6]. In simulating realistic breakup events in this study, we will consider a reference scenario with the initial conditions of an explosion event involving a spacecraft (as opposed to a rocket body) of varying mass from 50 to 1000 kg on a planar $L_2$ Lyapunov orbit. The minimum fragment size considered has been limited to 5 cm to reduce the computational burden, while the largest fragment length is fixed at 1 m. The breakup epoch is arbitrarily selected as 2023-08-29 00:00:00, although we acknowledge that the relative positions of the Sun, Earth, and Moon affect the final velocities of each fragment coming out of the breakup algorithm, and therefore breakup epoch conditions deserve further investigation. The initial conditions are summarized in Table 2.

Table 2: Breakup model initial conditions.

| | |
|---|---|
| **Event type** | explosion |
| **Debris type** | spacecraft |
| **Minimum fragment length** | 5 cm |
| **Maximum fragment length** | 1 m |
| **Breakup epoch** | 2023-08-29 00:00:00 |

#### 4.2.1 *Scale factor optimization*

Given the statistical nature of the model, no run will naturally produce an equal number of fragments or the same distribution of fragment characteristics. However, in order to reproduce a given case for continued analysis, the random number generator seed can be computationally fixed. This tactic is exploited in the implementation of the scale factor optimizer to obtain an optimal explosion scale factor for a satellite of any mass. Given the discontinuities present in the modified SBM model, the optimizer employs the Nelder-Mead simplex algorithm [15, 16] to find the minimum value of an unconstrained cost function. In order to limit the search to produce only scale factors that yield total fragment mass values less than that of the original satellite (prior to conservation of mass), a penalty is applied to the cost function when the mass requirement is not met. Since optimization requires repeatable results to obtain a solution, the random seed can be fixed. However, to maintain a random area-to-mass distribution model, a single seed is not appropriate, thus in that case an array of fixed seed values is assigned to the optimizer. The optimization function is executed prior to running the full breakup model, and the resulting scale factor and associated seed are applied to the model.

#### 4.2.2 *Sensitivity analysis*

Before embarking on a study of a specific breakup event, it is valuable for us to understand the relationships between some of the variables in our system. In a case, such as this, with a large parameter space, a sensitivity study can help identify inputs that are most responsive to changes and give overall insight into the parameters that have the largest influence on the system.

We can consider eighteen orbits and fifty true anomaly locations around each orbit, as well as two different satellite masses, to evaluate which of those parameters is most influential on the energy levels and rotational velocity magnitudes of the generated fragments. Running the breakup model without subsequent propagation is not computationally burdensome and yields valuable insight. Using the initial event conditions provided in Table 2, the breakup model is run only once per mass value, to maintain consistency in the analysis. As the algorithm is a function of spacecraft mass, the fragment outputs will differ between cases of different masses. The ejection velocity of each fragment produced by the modified SBM is then added to the initial velocity state of the spacecraft at the designated breakup location to obtain the final velocity and Jacobi constant of each debris object. The optimized scaled factor for the two mass cases and the number of explosion fragments generated are provided in Table 3.

Table 3: Sensitivity study parameters, in addition to those listed in Table 2.

| **Satellite mass [kg]** | 50 | 500 |
|---|---|---|
| **Explosion scale factor, s** | 0.264453 | 1.1625 |
| **Number of generated fragments** | 197 | 838 |

Figure 9 reveals the effect of mass and initial breakup location on the median of all fragment Jacobi constants for both a 50 kg object and a 500 kg object. We see from the median and mean results in the left and center plots in Figure 9(a) and (b) that the Jacobi constant is very dependent on the orbit of origination, and not as dependent on location around the orbit, remaining fairly constant and symmetric throughout the orbit, except where the orbit pinches in at its closest flyby of the Moon. We observe from these plots that the median and mean plots are not exactly aligned. We can intuitively understand that since objects on larger orbits that travel further away from the Moon have higher energies than smaller family members, fragments generated on those higher-energy orbits will be imbued with larger energies as well. In contrast, the right plot in Figure 9(a), representing the standard deviations of the Jacobi constant distribution at each location, does not yield the same intuitive results. There is a lack of symmetry about the $x$-axis of the orbit, with much larger variations in energy at the negative true anomaly locations compared with the positive $\theta$ angle locations. By far the largest standard deviations occur again at the orbital pinch point, increasing drastically as $\theta$ approaches -180°. However, in the right plot of Figure 9(b), we see that standard deviations are relatively lower than that of the 50 kg object and symmetry in the plot is restored. Both mass cases reveal that average fragment energy levels do not vary considerably with initial satellite mass, although standard deviations are more variable.

From the rotational velocity magnitude contours, both the mean and median contour plots in the left and center plots of Figure 10(a) and (b) appear to match for both the 50 kg and 500 kg mass scenarios. In both cases, the mean velocity

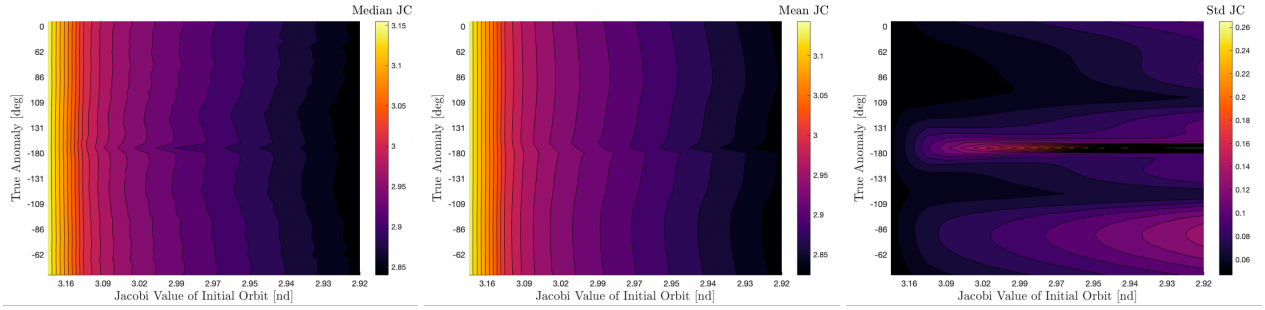


(a) Median (left), mean(center), and standard deviation (right) values of Jacobi constants for fragments generated from a 50 kg object.

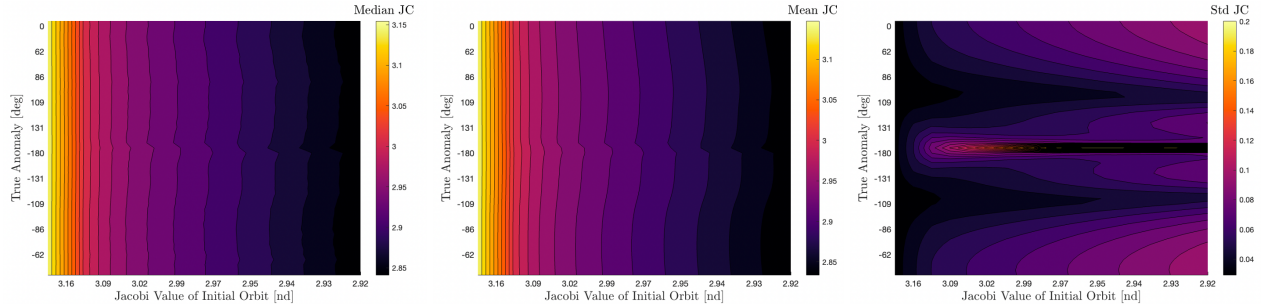


(b) Median (left), mean(center), and standard deviation (right) values of Jacobi constants for fragments generated from a 500 kg object.

Fig. 9: Contours representing changes in fragment Jacobi constants as a function of initial breakup location for satellites with two different mass values

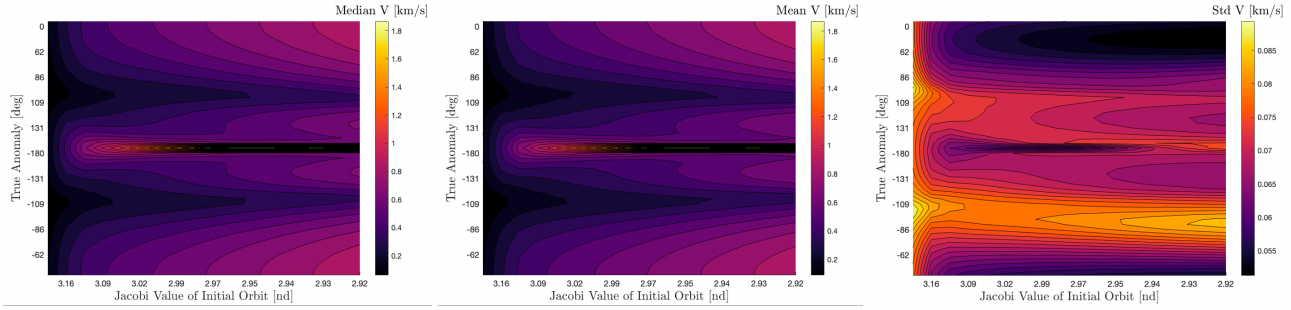


(a) Median (left), mean(center), and standard deviation (right) values of rotational velocity magnitude for fragments generated from a 50 kg object.

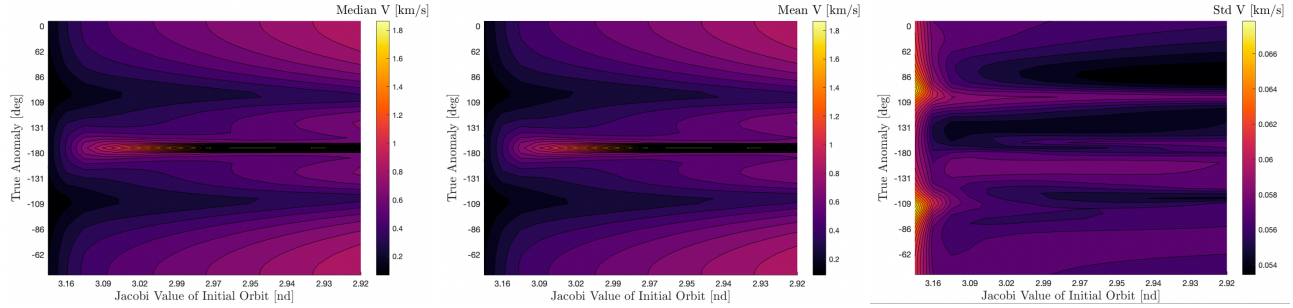


(b) Median (left), mean(center), and standard deviation (right) values of rotational velocity magnitude for fragments generated from a 500 kg object.

Fig. 10: Contours representing changes in fragment velocity magnitudes in the rotating frame as a function of initial breakup location for satellites with two different mass values

values reveal an almost perfect symmetry about the $x$-axis, although there is much more velocity sensitivity to changes in both orbit and true anomaly than there was with the energy terms. Higher velocity fragments look to exist for explosions originating close to the $x$-axis, as well as on higher energy orbits. However, once again, we observe unique behavior at the closest Moon pass of each orbit, with a sudden jump in fragment velocities. The standard deviations in velocity for the 50 kg object, in the right plot in Figure 10(a), look to be much larger on average than those for the 500 kg object, shown in the right plot in Figure 10(b). Neither plot is symmetric about $x$ and both exhibit spikes in standard deviation on smaller, lower energy orbits at a true anomaly of around $\pm 100^{\circ}$, which are located at the very top and bottom of the orbits. Once again, we observe almost no difference in average velocity magnitudes with changes in satellite mass, although differences exist in the velocity distribution standard deviations.

#### 4.2.3 *Reference breakup case*

We can now consider the effect of this analysis on a simulated breakup event, again using the input conditions specified in Table 2, and a satellite mass of 500 kg. Optimization of the explosion scale factor $s$ yields a value of 1.2187, which generates 881 pieces of debris. The explosion occurs when the satellite is at the nondimensional state of [1.2187 0 0 0 -0.4232 0], which corresponds to an object located at a position along the Earth-Moon $x$-axis and traveling in a negative $y$-direction on periodic planar $L_2$ Lyapunov orbit with a Jacobi value of 3.0165 and a dimensional period of 18.53 days.

The distributions obtained from the modified SBM model for the fragment characteristic lengths, area-to-mass ratios, masses, and delta-V magnitudes are displayed in Figure 11 along with their mean values. The shapes of the distributions are consistent with findings from literature [6, 8, 17]. The probability density of the rotational velocity magnitude

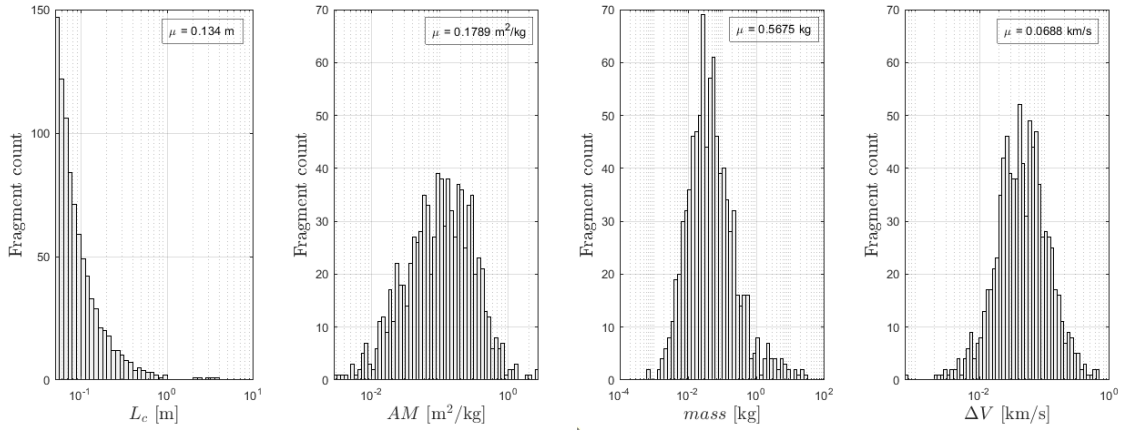


(a) Size distribution (b) Area-to-mass distribution (c) Mass distribution (d) Delta-V distribution

Fig. 11: Breakup model distributions for characteristic length $L_c$, area-to-mass ratio $AM$, mass, and ejection velocity $\Delta V$ of generated explosion fragments.

distribution is additionally included for reference in Figure 12, and indicates a mean fragment velocity of 0.456 km/s and standard deviation of 0.064 km/s. Recall that the SBM is a statistical algorithm, and, therefore, these distributions will not repeat each time the model is run. This leads to countless potential fragment velocities and energies for a single scenario, which is why it is valuable to identify repeatable behaviour and dynamical patterns.

Figure 13 displays the resulting fragments and associated trajectories corresponding to the explosion event described above. The fragments are color-coded based on their Jacobi constant, as indicated by the color bar in Figure 13(a). Figure 13(b) provides a three-dimensional view of the trajectories, while Figure 13(c) enables a closer inspection of trajectories nearby the orbit of origination. After 30 days of propagation, many of the fragments have travelled enormous distances, with some of the farthest reaching distances of up to 5.33 nd, or 2 million km, from their location of origination. We are able to identify one very large energy object that travels on a trajectory symmetric about the $x$-axis and collides with the Earth. Simulations like this prove that even with an explosion at 1.2187 nd, or 470,000 km, from the Earth, which generates less than one thousand pieces of debris, Earth reentries are possible, and even likely.

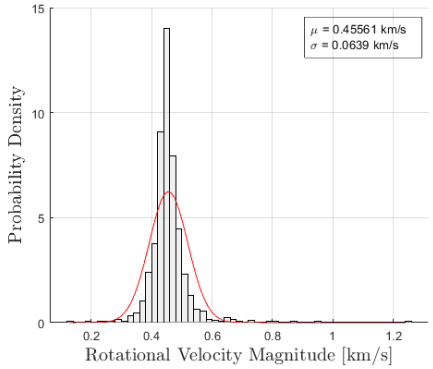


Fig. 12: Probability density distribution of fragment velocity magnitudes.

And with plans of colonizing the Moon on the horizon, the amount of Moon impacts due to only one fragmentation event will be unacceptable, especially given the lack of a lunar atmosphere to decelerate or destroy them.

Figure 14 provides a Jacobi-centered view of the fragment behaviour in this case. In Figure 14(a) the trajectory plot has been reevaluated in terms of energy regions, rather than individual Jacobi values. The regions have been defined according to the energy levels required to pass through the various Earth-Moon libration points. The first region, defined by the color yellow, represents objects with very low energies and Jacobi constants greater than that of the $L_1$ equilibrium point, such that they are incapable of traversing through $L_1$ and remain trapped on whichever side of the ZVC they originate from. The second region, represented by the color orange, indicates objects with Jacobi values between those of $L_1$ and $L_2$, denoting the ability to pass through $L_1$, but not $L_2$. The third, or red, region represents objects with Jacobi values between those of $L_2$ and $L_3$, such that $L_2$ is available for travel, but $L_3$ is not. The fourth region, in purple, includes objects with Jacobi values between those of $L_3$ and $L_4$. And finally, region five, displayed in black, encompasses fragments for which no ZVCs exist, and thus, fragments at those high energies can travel unhindered by dynamical boundaries.

Figure 14(a) provides insight into the energy regions in which each fragment lies. The more erratic trajectories belong to fragments without ZVCs and demonstrate their ability to move about freely in cislunar space. Figure 14(b) supplies a breakdown of the Jacobi distribution of the explosion. Those details are summarized in Table 4. As seen from the distribution, 31% of fragments belong to the fifth region, indicating that a third of the generated fragments have the potential for unpredictable travel patterns. Out of the remainder of fragments, 33% belong to the third region and 36% have energies in the fourth region, both of which face limited travel restrictions. Only 0.1% of fragments fall in the low energy categories. The fragments have an average *JC* of 2.994, a median *JC* value of 3.002, and a *JC* standard

Table 4: *JC* region summary.

| **Region** | **Jacobi range** | **Fragment percentage** |
|---|---|---|
| Yellow region | $> 3.1883$ | 0% |
| Orange region | 3.1722 - 3.1883 | 0.1% |
| Red region | 3.0121 - 3.1722 | 33% |
| Purple region | 2.9880 - 3.0121 | 36% |
| Black region | $< 2.9880$ | 31% |

deviation of 0.071. If we attempt to correlate those values to the *JC* plots associated with a 500 kg object in Figure 9(b), on an orbit with a *JC* of 3.0165, and a true anomaly of 0°, we would expect to get an average *JC* of around 2.96, and a standard deviation of around 0.07, which align reasonably well with the findings in the sample scenario. Figure 14(c) displays the Poincaré map for this fragmentation event on a hyperplane located at the halfway point between $L_2$ and the Earth. From looking at the trajectory plots in Figures 13(a) and 14(a), similar to the earlier analysis of constant *JC* conditions, we observe that many of the fragments, especially those with lower energies, look to be traveling on clearly defined invariant manifolds. Interestingly, these manifolds appear to remain mostly planar and thus do not form the visually gratifying egg-shaped three-dimensional manifolds explored in Section 4.1.

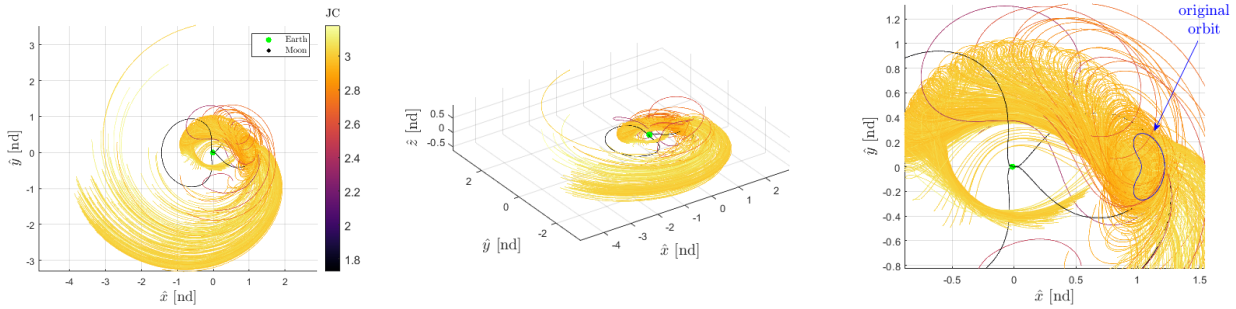


(a) Fragment trajectories after 30 days

(b) Three-dimensional view

(c) Closer look at the region near the original orbit and the Earth

Fig. 13: Fragment trajectories generated by a simulated explosion on an $L_2$ Lyapunov orbit. Fragments are color-coded by Jacobi constant.

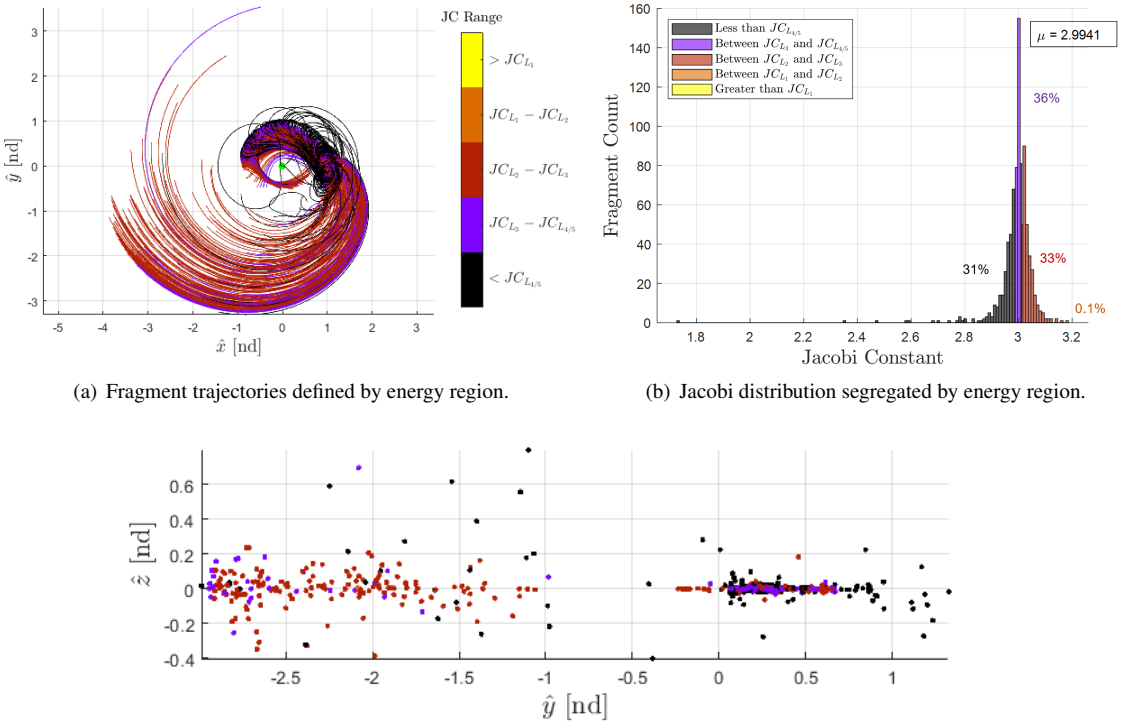


(a) Fragment trajectories defined by energy region.

(b) Jacobi distribution segregated by energy region.

(c) Position space Poincaré map at the halfway point between the Earth and $L_2$.

Fig. 14: Summary of reference explosion scenario, with outputs classified according to energy range categories.

## 5. CONCLUDING REMARKS

With increased interest in lunar missions, and heightened activity in the Cislunar region, a focus on understanding the complex multibody dynamics of fragmentation events without exorbitant computational expense is necessary for the support of debris mitigation strategies. In this investigation, the motion of fragments characterized by constant energies is explored and subsequent dynamical structures are examined. Multiple breakup locations in the vicinity of the $L_2$ Lagrange point are investigated, and behavioral patterns specific to the location of the breakup are found to exist. Zero Velocity Curves (ZVCs) and manifolds provide some measure of predictability in fragment motion, although ZVCs become irrelevant at higher energies. A sensitivity analysis is performed on satellites of different masses to look at the factors that characterize a fragmentation event and their influence on the Jacobi constant and fragment

velocity magnitude. Little variation is found to exist between masses, while the orbit of origination is seen to be the largest influence on fragment energies. Finally, a physically realistic explosion event is modeled using a modified version of the NASA Standard Breakup Model, and insight gleaned from the constant energy study is applied in the analysis, although some different behavior is exhibited relative to the theoretical constant Jacobi cases. Notably, the average energy levels of a realistic explosion are often large enough to enable fragments to move unhindered throughout cislunar space. Grouping the fragmentations into respective Jacobi constant regions enables the prediction of allowable pathways without the need for propagation.

## ACKNOWLEDGMENTS

The authors would like to thank Dr. Kathleen Howell for the fruitful discussions and insightful guidance.

## REFERENCES

[1] M.J. Holzinger, C.C. Chow, and P. Garretson. *A Primer on Cislunar Space*. Air Force Research Laboratory, 2021.

[2] National Aeronautics Space Administration. The moon.

[3] Chunlai Li, Wei Zuo, Weibin Wen, Xingguo Zeng, Xingye Gao, Yuxuan Liu, Qiang Fu, Zhoubin Zhang, Yan Su, Xin Ren, et al. Overview of the chang'e-4 mission: Opening the frontier of scientific exploration of the lunar far side. *Space Science Reviews*, 217:1–32, 2021.

[4] Bradley Cheetham. Cislunar autonomous positioning system technology operations and navigation experiment (capstone). In *ASCEND 2021*, page 4128. 2021.

[5] Donald J Kessler. The kessler syndrome as discussed by donald j. kessler, 2009.

[6] Nicholas L Johnson, Paula H Krisko, J-C Liou, and Phillip D Anz-Meador. Nasa's new breakup model of evolve 4.0. *Advances in Space Research*, 28(9):1377–1384, 2001.

[7] Arly Black and Carolin Frueh. Investigation of fragmentation events in the cislunar domain. In *AAS/AIAA Space Flight Mechanics Meeting*, Austin, TX, January 2023.

[8] Paolo Guardabasso, Despoina K Skoulidou, Lorenzo Bucci, Francesca Letizia, Stijn Lemmens, Marie Ansart, Xavier Roser, Stéphanie Lizy-Destrez, and Grégoire Casalis. Analysis of accidental spacecraft break-up events in cislunar space. *Advances in Space Research*, 2023.

[9] Nathan R Boone and Robert A Bettinger. Debris collision risk analysis following simulated cislunar spacecraft explosions. *Journal of Spacecraft and Rockets*, 60(2):668–684, 2023.

[10] Victor Szebehely and E Grebenikov. Theory of orbits-the restricted problem of three bodies. *Soviet Astronomy, Vol. 13, p. 364*, 13:364, 1969.

[11] PH Krisko. Proper implementation of the 1998 nasa breakup model. *Orbital Debris Quarterly News*, 15(4):1–10, 2011.

[12] A Horstman et al. Enhancement of s/c fragmentation and environment evolution models. *Final Report, Contract N. 4000115973/15/D/SR, Institute of Space System, Technische Universität Braunschweig*, 26(08), 2020.

[13] Gerard Gómez, Wang S Koon, Martin W Lo, Jerrold E Marsden, Josep Masdemont, and Shane D Ross. Connecting orbits and invariant manifolds in the spatial restricted three-body problem. *Nonlinearity*, 17(5):1571, 2004.

[14] KC Howell, M Beckman, C Patterson, and D Folta. Representations of invariant manifolds for applications in three-body systems. *The Journal of the Astronautical Sciences*, 54:69–93, 2006.

[15] Jeffrey C Lagarias, James A Reeds, Margaret H Wright, and Paul E Wright. Convergence properties of the nelder–mead simplex method in low dimensions. *SIAM Journal on optimization*, 9(1):112–147, 1998.

[16] MATLAB. *Optimizing Nonlinear Functions*. The MathWorks Inc., Natick, Massachusetts.

[17] A Rossi, G Koppenwallner, PH Krisko, M Oswald, and M Xu. Nasa breakup model implementation comparison of results. In *24th IADC Meeting*. IADC, 2006.